ARTICLES
PUBLISHED ONLINE: 14 MARCH 2016 | DOI: 10.1038/NMAT4585
nature materials

Paramagnetic fluorinated nanoemulsions for sensitive cellular fluorine-19 magnetic resonance imaging

Alexander A. Kislukhin[1], Hongyan Xu[2], Stephen R. Adams[1], Kazim H. Narsinh[2], Roger Y. Tsien[1,3,4]* and Eric T. Ahrens[2]*

Fluorine-19 magnetic resonance imaging (^{19}F MRI) probes enable quantitative *in vivo* detection of cell therapies and inflammatory cells. Here, we describe the formulation of perfluorocarbon-based nanoemulsions with improved sensitivity for cellular MRI. Reduction of the ^{19}F spin–lattice relaxation time (T_1) enables rapid imaging and an improved signal-to-noise ratio, thereby improving cell detection sensitivity. We synthesized metal-binding β-diketones conjugated to linear perfluoropolyether (PFPE), formulated these fluorinated ligands as aqueous nanoemulsions, and then metallated them with various transition and lanthanide ions in the fluorous phase. Iron(III) *tris*-β-diketonate ('FETRIS') nanoemulsions with PFPE have low cytotoxicity (<20%) and superior MRI properties. Moreover, the ^{19}F T_1 can readily be reduced by an order of magnitude and tuned by stoichiometric modulation of the iron concentration. The resulting ^{19}F MRI detection sensitivity is enhanced by three- to fivefold over previously used tracers at 11.7 T, and is predicted to increase by at least eightfold at the clinical field strength of 3 T.

Magnetic resonance imaging (MRI) is becoming a clinical tool for visualizing specific cell populations in the body[1]. MRI cell detection using exogenous agents can be used to visualize the *in vivo* trafficking and behaviour of immune or stem cells used to treat a host of diseases. Fluorine-19 (^{19}F) 'tracer' agents are an emerging approach to intracellularly label cells of interest, either *ex vivo* or *in situ*, to enable cell detection by means of ^{19}F MRI (refs 1,2). The ^{19}F label yields positive-signal 'hotspot' images, with no background signal owing to negligible fluorine concentration in tissues. Images can be quantified to measure apparent cell numbers at sites of accumulation[2,3], thereby enabling '*in vivo* cytometry'[4]. Tracer agent compositions have mostly focused on non-toxic perfluorocarbons (PFCs). Clinical translation of ^{19}F cell detection has recently been realized in patients[5] using PFC nanoemulsion to label a dendritic cell cancer vaccine; in these experiments, the cell detection limit was conservatively estimated to be of the order of 10^5 cells per voxel[5].

Improving the sensitivity of ^{19}F cell detection could lower the barriers for using this technology in a wider range of biomedical applications. One approach for boosting sensitivity is by decreasing the intrinsically high ^{19}F spin–lattice relaxation time (T_1) of PFC molecules[6–8]. The T_1 ultimately limits the rate of ^{19}F MRI data acquisitions. Often, ^{19}F images require summation of multiple acquisitions (that is, signal averaging) to generate a sufficient signal-to-noise ratio (SNR) for confident interpretation. High ^{19}F T_1 values require a long repetition time (TR) to allow for longitudinal signal recovery, thus limiting the number of signal acquisitions attainable during a fixed total imaging time (t_i). As t_i is constrained when scanning patients, the key parameter to maximize is SNR/t_i. Shortening T_1 can increase SNR/t_i, sensitivity, and decrease the minimum number of detectable cells per voxel. In practice, reducing T_1 by molecular design can also lead to a reduction in the spin–spin relaxation time (T_2) and line broadening of the resonance; this effect may degrade the SNR if T_2 becomes comparable to the data acquisition sampling time along the frequency-encoding direction[9]. The creation of stable and cytocompatible ^{19}F agents with 'ultrafast' T_1 is an open challenge that can greatly impact the MRI field, enabling accelerated MRI acquisitions and the detection of sparser cell populations *in vivo*.

The relaxation times T_1 and T_2 can be profoundly altered by high-spin paramagnetic metal ions (for example, Mn^{2+}, Fe^{3+}, Gd^{3+}). Previous studies[6] have attached Gd^{3+} to the outer surface of the PFC nanoemulsion droplet resulting in modest reductions in T_1. With increasing distance (r), the steep fall-off ($\sim r^{-6}$) of paramagnetic relaxation rate enhancement from paramagnetic centres limits the efficacy of relaxation agents bound to the surface of PFC nanoparticles[8,10]. Thus, effective relaxation enhancement necessitates introduction of metal ions into the fluorous phase, that is, within the nanoemulsion droplets, to achieve a short T_1 using a minimum amount of a paramagnetic additive.

We describe the scalable synthesis and properties of a family of paramagnetic PFC nanoemulsions with excellent ^{19}F MRI and biological properties. We show that fluorinated materials incorporating suitable ligands can tightly bind and retain sufficient amounts of metal ions in the fluorous phase of the nanoemulsion to yield ^{19}F agents with greatly enhanced sensitivity. These new nanoemulsion materials contain metal-binding β-diketones conjugated to linear perfluoropolyether (PFPE). Using these agents, we describe preliminary assessments of the biocompatibility, cell labelling stability, and *in vivo* MRI studies in mice. Sensitivity

[1]Department of Pharmacology, University of California, San Diego, La Jolla, California 92093, USA. [2]Department of Radiology, University of California, San Diego, La Jolla, California 92093, USA. [3]Department of Chemistry and Biochemistry, University of California, San Diego, La Jolla, California 92093, USA. [4]Howard Hughes Medical Institute, University of California, San Diego, La Jolla, California 92093, USA. *e-mail: rtsien@ucsd.edu; eahrens@ucsd.edu

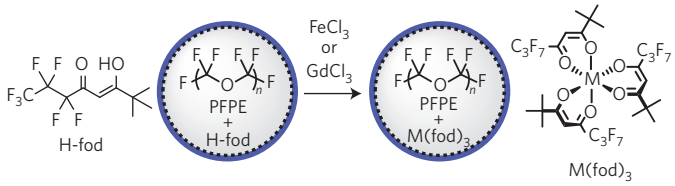

Metal (M)	None	Fe	Gd
R_1 (s^{-1})	2.28 ± 0.01	27.0 ± 0.1	12.8 ± 0.2
R_2 (s^{-1})	4.01 ± 0.03	85.6 ± 0.2	285 ± 3
R_2/R_1	1.8	3.2	22

Figure 1 | Comparison of iron and gadolinium diketonates (H-fod) as ^{19}F relaxation agents for PFPE. The relaxometry results (9.4 T) are shown for PFPE emulsions (120 g l^{-1} PFPE) containing H-fod (2.8 mM) 24 h after the addition of 0.7 mM metal ions. R_1, spin–lattice relaxation rate (=$1/T_1$), and R_2, spin–spin relaxation rate (=$1/T_2$), values are reported for the main PFPE peak at −91.4 ppm. The results show that Fe^{3+} is a more effective R_1 agent than Gd^{3+}.

enhancement of these materials will potentially accelerate the use of ^{19}F cell detection in a host of clinical cell therapy trials and for diagnostic inflammation imaging.

Modelling of paramagnetic relaxation enhancement

In the initial design of ^{19}F probes, we conducted magnetic resonance relaxation time modelling of the impact of dissolving metal ions into PFC. Solomon–Bloembergen–Morgan (SBM) theory[11,12] describes paramagnetic relaxation enhancement (PRE) of $R_1 = 1/T_1$ and $R_2 = 1/T_2$ of surrounding media at a given magnetic field strength, molecular mobility, and metal concentration (see Supplementary Information). Using SBM theory, we found optimal parameters for enhancement of R_1 while minimizing linewidth broadening, that is, R_2. The modelling results (Supplementary Fig. 1) show that Fe^{3+} uniformly dispersed in PFC will provide the most robust enhancement of ^{19}F R_1. Mn^{2+} and Gd^{3+} are likely to cause severe line broadening due to a large increase in R_2, especially at high magnetic field strengths. This line broadening originates from very slow electronic relaxation in Mn^{2+} and Gd^{3+} (Supplementary Fig. 1).

Design and preparation of metal-binding perfluorocarbons

Design of a cytocompatible fluorous-soluble metal chelate requires careful consideration. The steep fall-off of PRE with increasing distance ($\sim r^{-6}$) necessitates solubilization of individual metal ions, as opposed to incorporating metal-bearing oligomeric clusters or nanoparticles. The metal must not efflux from the fluorous phase during cell labelling and after *in vivo* administration. The high electronegativity of fluorine imparts very low cohesive energy density[13] and Lewis basicity[14] to heavily fluorinated compounds, making them extremely poor solvents and ligands. The choice of ligands compatible with fluorous phase is therefore limited to the most hydrophobic scaffolds, with as few intermolecular interactions as possible. To maximize solubility in the fluorous phase, the resulting metal complex should be uncharged and coordinatively saturated. These criteria can be satisfied by using bidentate, monoionic ligands (L) that form high-spin, charge-neutral *tris*-complexes with trivalent metals (FeL_3, GdL_3) and *bis*-complexes with divalent metals (MnL_2). Of these, only FeL_3 complexes are coordinatively saturated, owing to the small size of the parent Fe^{3+} ion. Coordinatively unsaturated complexes of larger Mn^{2+} and Gd^{3+} tend to be unstable with respect to the formation of oligomeric[15], charged or ternary complexes[16] (for example, $[GdL_3]_n$, $[GdL_4]^-$, $[GdL_3 \cdot (H_2O)_x]$). Although gadolinium chelates are widely used contrast agents in clinical ^{1}H MRI because Gd^{3+} has the highest magnetic moment, we predict that Fe^{3+} is better suited for ^{19}F applications.

Initially, we tested the results of the PRE modelling (see Supplementary Fig. 1) using small molecules. Fluorinated β-diketone H-fod (Fig. 1) was chosen as the starting point. Addition of 2.8 mM H-fod to the aqueous phase of a pre-made PFPE nanoemulsion resulted in apparent dissolution of the diketone and the appearance of heptafluoropropyl groups in ^{19}F nuclear magnetic resonance (NMR) spectra featuring three broad singlets. Addition of 0.7 mM $FeCl_3$ led to the slow formation of orange-coloured $Fe(fod)_3$ and a commensurate increase in R_1 from 2.3 to 27.0 s^{-1} and in R_2 from 4.0 to 85.6 s^{-1} (at 9.4 T) of the main PFPE resonance (−91.4 ppm) by 24 h (Supplementary Fig. 3). With $GdCl_3$, lower R_1 (12.8 s^{-1}) and higher R_2 (285 s^{-1}) values were obtained. The corresponding gadolinium complex exhibited modest R_1 values accompanied by strong line broadening, a likely consequence of both the high electronic relaxation time (T_{1e}) of Gd^{3+} and the high rotational correlation time (τ_R) of the oligomeric gadolinium chelate (see Supplementary Equations (1)–(4) and Supplementary Figs 1 and 2). However, broad NMR signals of the ligand in the absence of metals and slow metallation kinetics suggested insufficient solubility of H-fod in PFPE.

To improve solubility, we investigated fluorinated β-diketones (FDKs) that have a greater fluorine content. We prepared the PFPE-based ligand pAn-FDK using Claisen condensation[17] between PFPE-OMe and excess *p*-methoxyacetophenone, yielding highly pure pAn-FDK product at >10 g scale on simple extractive workup (Fig. 2a). ^{1}H NMR analysis revealed new peaks at 6.46 and 15.35 ppm, characteristic of a diketone in enol form (Supplementary Fig. 4). This ligand was used for subsequent studies.

To evaluate ^{19}F MRI properties, we blended pAn-FDK with a variety of perfluorocarbon derivatives and formulated these blended oils into aqueous nanoemulsions using microfluidization. Nanoemulsions (Fig. 2c) included pAn-FDK alone (emulsion A), or as a blend with PFPE diethylamide (DEA) (B), PFPE (D), perfluorooctyl bromide (PFOB) (F), or a short PFPE oligomer perfluorotetraglyme (PF4G) (G). Emulsions C (pure PFPE-DEA) and E (pure PFPE) are controls that cannot bind metals (Fig. 2c). We note that PFOB was tested because of its rapid clearance from the body and previous use clinically, but it is not preferred for MRI cell detection owing to its multiple ^{19}F resonances that diminish image quality[18]. In all formulations A–G, stable nanoemulsions were formed, with similar physical characteristics. Dynamic light scattering measurements in A–G revealed monodisperse nanoemulsions with a polydispersity index of <0.2 and average droplet diameters ranging from 140 to 200 nm and negative ζ-potentials of −27 to −56 mV (Supplementary Fig. 5). No change in dynamic light scattering measurements was noted for up to 8 months of storage at 4 °C. Nanoemulsion composition was confirmed by ^{19}F NMR (Fig. 2d). Terminal CF_2 atoms of PFPE derivatives have resonances between −70 and −85 ppm. Presence of only one major peak in this spectral range in single-component emulsions A and C confirmed high purities of the starting oils; emulsion B shows peaks from both components in the expected 1:1 ratio. Core CF_2CF_2O units resonating at −91 ppm comprise ∼90% of the total ^{19}F spectral weight and this is typically the only signal detectable by ^{19}F MRI, which generally has a much lower SNR compared with conventional ^{1}H images.

Properties of metallated nanoemulsions

The Pluronic surfactant used in the nanoemulsion formulation is permeable to ions enabling direct metallation of FDK nanoemulsions by the addition of metal chloride into the aqueous phase (Fig. 2e). Optical changes due to the formation of metal complexes were readily observed (Fig. 2f and Supplementary Fig. 6). Among these, europium chelates are notable for their bright photoluminescence, which may be useful for studying intracellular localization and trafficking of the PFC droplets (Supplementary Fig. 11e). Importantly, addition of $FeCl_3$ caused

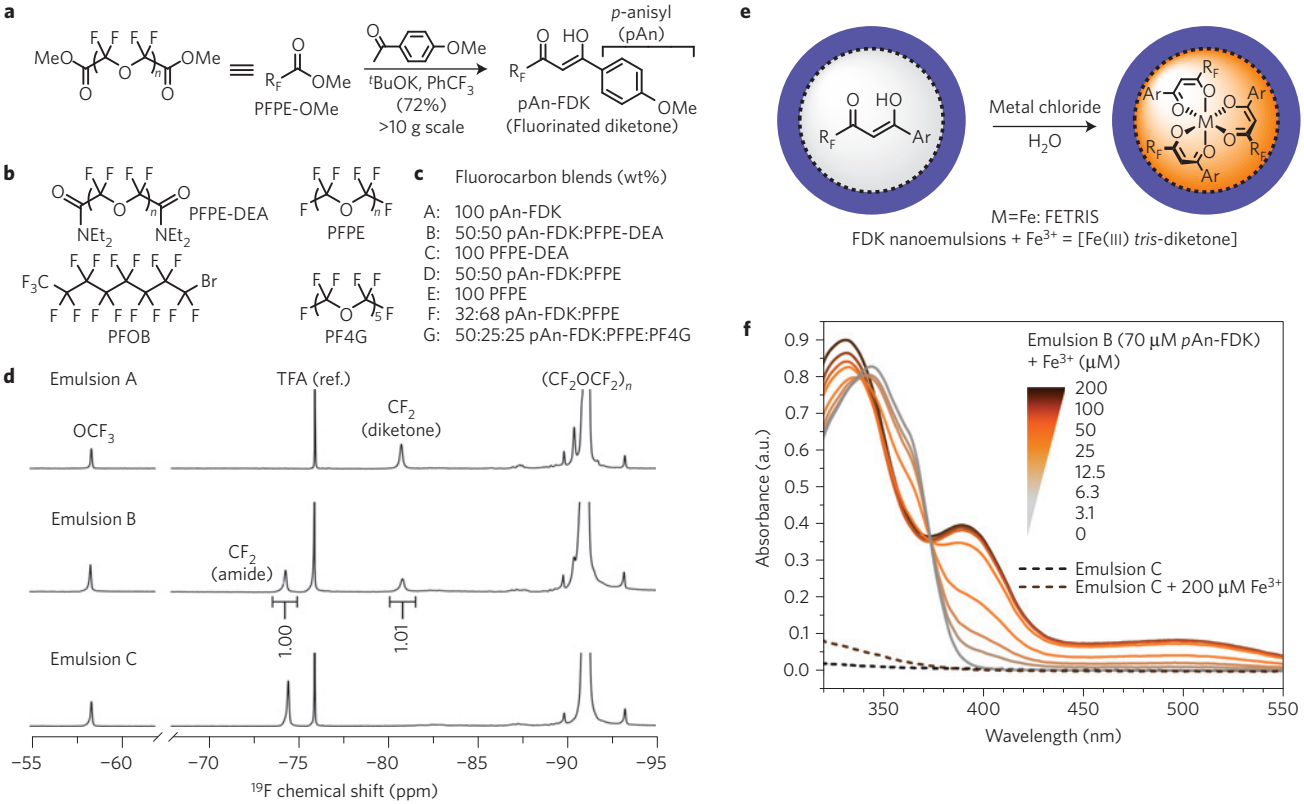

Figure 2 | Preparation and characterization of metal-binding nanoemulsions for ^{19}F MRI. a, Synthesis of metal-binding fluorinated diketones (FDK) from PFPE-OMe (denoted as R_FCO_2Me). The average number of (CF_2OCF_2) repeats (n) is 12. tBuOK, potassium *tert*-butoxide; $PhCF_3$, trifluorotoluene; 72% yield based on PFPE-OMe. **b**, Structures of fluorocarbons used for ^{19}F MRI. **c**, Composition and preparation of various metal-binding (A, B, D, F, G) and control (C, E) fluorocarbon nanoemulsions. **d**, ^{19}F NMR spectra (11.7 T) of emulsions A–C (4.5 g l^{-1} ^{19}F, 90% D_2O). Signals from terminal CF_2 of diketone ligands are well separated from other peaks and are used to determine ligand concentration. The peak at −76 ppm is the reference (CF_3CO_2Na, TFA). The two values indicate the integrated signal intensity in integration units. **e**, Addition of aqueous metal chlorides to FDK emulsions yields metallated emulsions; Ar: *p*An. **f**, Absorption spectra of metal-binding emulsion B (70 μM diketone, 0.09 g l^{-1} ^{19}F) (coloured lines) and control emulsion C (0.09 g l^{-1}) (dashed lines) with and without of Fe^{3+}. Increasing [Fe^{3+}] causes the appearance of ferric *tris*-diketonate charge transfer bands at 395 and 500 nm, which grow linearly in intensity until a ratio of approximately 3:1 ligand/Fe is reached at 25 μM Fe^{3+}.

rapid ($k_{obs} = 0.69 \pm 0.10\ min^{-1}$) appearance (Supplementary Fig. 7) of characteristic charge transfer bands of ferric diketonates[19] ($\varepsilon_{390} = 23$, $\varepsilon_{500} = 4.9\ mM^{-1}\ cm^{-1}$) that linearly increased in intensity with increasing [Fe^{3+}] until the Fe/FDK ratio of about 1:3 was reached, consistent with ferric *tris*-diketonate (Fig. 2f). Henceforth, the term 'FETRIS' (from ferric *tris*-diketonate) refers to pAn-FDK blended with PFPE and metallated with Fe^{3+}.

Relaxometric evaluation of nanoemulsions in the presence of different metals (Fig. 3a) revealed that binding of Fe^{3+} resulted in modest line broadening of all ^{19}F NMR resonances, including the main PFPE peak at −91 ppm. The highest R_1 observed ($158.2 \pm 2.5\ s^{-1}$ at 11.7 T), with a linewidth of 4 kHz, was with FETRIS saturated with Fe^{3+}. Despite the largest number of unpaired electrons, Gd^{3+} showed a twofold lower R_1 compared with Fe^{3+}, with severe line broadening. Mn^{2+} gave moderately broad signals with the lowest R_1 of the triad. To confirm that the linewidth of metallated nanoemulsions is dominated by paramagnetism and not by metal binding per se, diamagnetic Ga^{3+}, with a similar ionic radius to Fe^{3+}, was included in the analysis and was found to have R_1 and R_2 equal to $2.08 \pm 0.01\ s^{-1}$ and $20.9 \pm 0.3\ s^{-1}$, respectively; this small change in relaxation rates relative to the unmetallated emulsion, with $R_1 = 2.37 \pm 0.01\ s^{-1}$, and $R_2 = 15.1 \pm 0.2\ s^{-1}$ (9.4 T), is attributable to an increase in the effective molecular weight on formation of the metal complex.

We determined the phase distribution of the paramagnetic ions and the metal-binding capacity of FDK nanoemulsions (Fig. 3b). Measurement of R_1 at 11.7 T for both PFPE (fluorous phase) and trifluoroacetate reference (TFA) added to the aqueous phase revealed that nanoemulsions efficiently extracted Gd^{3+} and Fe^{3+} from water into the fluorous phase. R_1 of PFPE reached a plateau at a ligand-to-metal ratio of about 2.5; increasing metal concentration further affected the R_1 of TFA. Notably, an increase in R_1 of TFA was observed even at the lowest Gd^{3+} concentration in pure PFPE nanoemulsion, confirming that the paramagnetic ion stays in the aqueous phase. We speculate that the modest (~2-fold) increase in R_1 of PFPE in this case was likely to be due to binding of Gd^{3+} ions to the nanoemulsion surface[8,10]. We observed a divergent field and temperature dependence of R_1 and R_2 in FETRIS nanoemulsions (Fig. 3c,d and Supplementary Fig. 8). Further control over relaxation parameters was achieved by tuning molecular weight and viscosity of the emulsion components (Supplementary Fig. 9). Other rare earths had only a minor effect on R_1, consistent with fast electronic relaxation in these metal ions[20] (Supplementary Fig. 10).

We also evaluated the stability of metal–FDK complexes. Using metal-loaded nanoemulsion, we monitored changes in photoluminescence (Eu^{3+}) and absorbance (Fe^{3+}) in the presence of excess competing ligands to study potential leakage of metal from the fluorous phase. Ethylenediaminetetraacetate (EDTA), a strong metal chelator[21], rapidly (<5 min) abolished the photoluminescence of europium-loaded emulsion owing to complete sequestration of Eu^{3+} to the aqueous phase to form a non-photoluminescent EDTA complex. In contrast, FETRIS nanoemulsion showed no decrease in

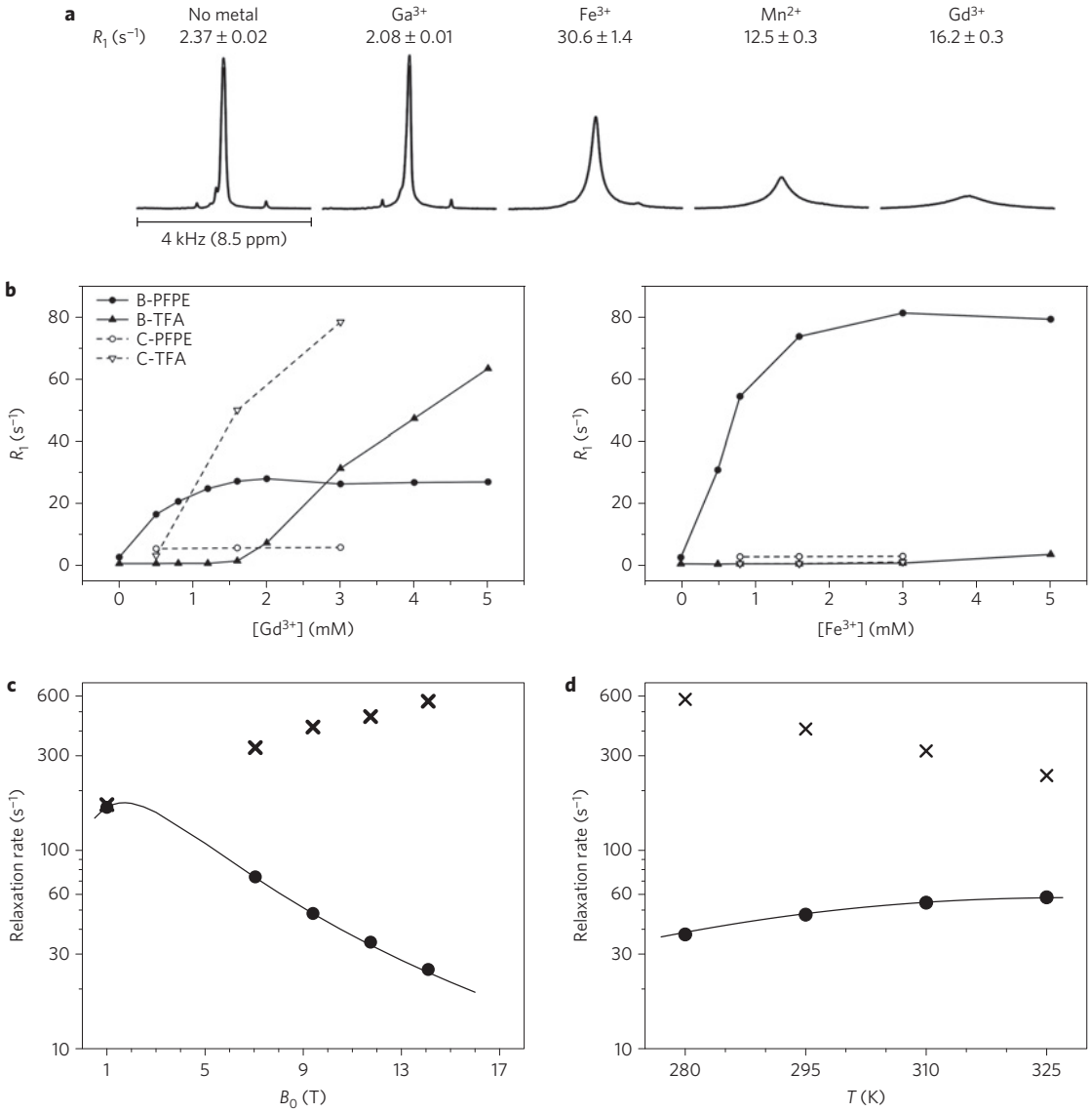

Figure 3 | Fluorine-19 relaxometry of metallated PFPE emulsions. a, R_1 and ^{19}F NMR spectra of FETRIS nanoemulsion (4.5 g l^{-1} ^{19}F, 3.5 mM diketone) in the presence of 0.5 mM metal ions, 15 mM HEPES and at pH 7.4. The peaks from different ^{19}F spectra are scaled to the same absolute intensity. **b**, Relaxometric analysis of Fe^{3+} and Gd^{3+} binding capacity. Shown are measurements of R_1 for both PFPE (fluorous phase) and trifluoroacetate reference (TFA) added to the aqueous phase. **c**,**d**, Magnetic field dependence at $T = 295$ K (**c**) and temperature (magnetic field strength, $B_0 = 9.4$ T) dependence (**d**) of observed relaxation rates R_1 (filled circles) and R_2 (crosses) in FETRIS nanoemulsion (22.5 g l^{-1} ^{19}F, 17.5 mM diketone, 2.8 mM Fe^{3+}) and predicted R_1 (line) values using Supplementary Equations (1)–(4). Predicted R_1 values represent the best fit to SBM equations, with $r = 1.19$ nm, τ_F (295 K) = 0.80 ns, vibrational correlation time τ_v (295 K) = 3.59 ps, and with Arrhenius temperature dependence activation energies of 3.6 kcal mol^{-1} for τ_F and 4.5 kcal mol^{-1} for τ_v. The diamagnetic contributions to R_1 are presumed to be negligible and Δ is fixed at 0.2 cm^{-1}. R_1 values increase, whereas R_2 values decrease, at lower magnetic field strengths, suggesting that there will be no degradation of the SNR at clinical fields due to line broadening.

characteristic absorbance of the Fe^{3+} chelate, even with prolonged exposure to EDTA. To estimate long-term stability of FETRIS nanoemulsions, relaxation rates were measured in the presence of EDTA (Fig. 4). PFPE-based nanoemulsion showed <20% decrease in R_1 over two weeks of incubation at 37 °C with EDTA.

Next, we examined FETRIS nanoemulsion properties in labelled cells. *Ex vivo* labelling of a rodent glioma cell line (GL261) with FETRIS showed good viability post-labelling (Fig. 5a), with loadings of the order of $\sim 10^{12}$ ^{19}F atoms per cell (Fig. 5b). Uptake of FETRIS was evident by the orange colour of cell pellets, and optical absorbance in the lysate correlated with the ^{19}F content determined by NMR (Fig. 5c). Fluorine-19 relaxometry of labelled cells (Supplementary Fig. 11) showed that FETRIS nanoemulsion did not seem to lose Fe^{3+} to the intracellular milieu over time; moreover, in the same nanoemulsion formulated without added Fe^{3+}, it did not seem to sequester endogenous Fe^{3+} from the cell's labile iron pool (Supplementary Fig. 11c). However, Gd^{3+} substituted for Fe^{3+} in the nanoemulsion showed evidence of some metal leakage on cell labelling; we observed about 25% reduction of ^{19}F R_1 values after labelling (Supplementary Fig. 11d).

Magnetic resonance imaging with FETRIS

Phantom ^{19}F MRI studies demonstrated the feasibility of imaging FETRIS using conventional MRI methods. A phantom sample was prepared consisting of two NMR tubes containing FETRIS prepared with parameters $R_1/R_2 = 32.5/170\ s^{-1}$ and the same emulsion without metal ($R_1/R_2 = 2.2/3.7\ s^{-1}$); tubes were embedded in agarose. Images were acquired at 11.7 T using a spin-density-

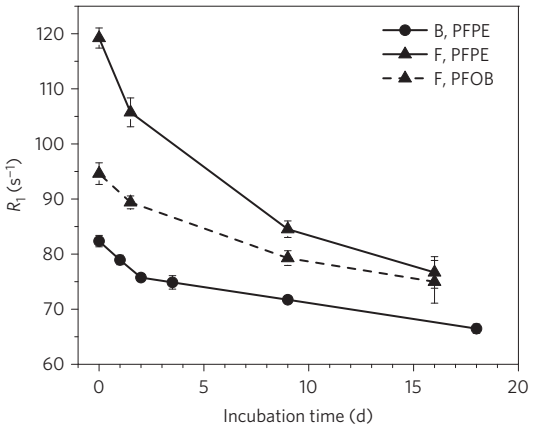

Figure 4 | Relaxometry stability of FETRIS nanoemulsions in the presence of competing aqueous ligand. Nanoemulsions B and F, both metallated with 0.7 mM Fe^{3+}, were treated at 37 °C with 75 mM EDTA dissolved in aqueous phase. Shown are R_1 values of PFPE (solid line with filled circles) in nanoemulsion B, and values for blend nanoemulsion F, including PFPE components (solid line with filled triangles) and the CF_3 signal of PFOB (dashed line with filled triangles). A slight decrease over time is observed, as slow Fe^{3+} efflux occurs from the fluorous phase and irreversibly binds to EDTA. Error bars are standard deviations from three independent replicates.

weighted gradient echo (GRE) sequence, with scanning parameters set at the Ernst angle condition[9] for optimal imaging of the FETRIS specimen, and a ~4 min image acquisition time. Figure 6a shows phantom MRI results, where the FETRIS sample seems hyperintense; the measured ^{19}F image SNRs for FETRIS and Fe-negative specimens were 8.6 and 1.7, respectively, yielding a SNR improvement of ~5 for the FETRIS sample, without Rician correction for the low SNR regime[3]. If each capillary was imaged using its appropriate Ernst angle, the SNR improvement would be ~3.3 (see modelling results, Supplementary Fig. 12). To further minimize potential T_2 signal loss when imaging FETRIS agents, one could potentially use so-called ultrashort TE (echo time) or zero TE (ZTE) pulse sequences[7]. Pulse sequences such as GRE are commonplace on clinical scanners, whereas ZTE is not yet readily provided by MRI vendors.

Preliminary *in vivo* imaging of FETRIS-labelled cells was performed. Glioma cells were labelled with FETRIS nanoemulsion (50 wt% pAn-FDK, 50 wt% PFPE) *ex vivo* to a level of ~10^{12} ^{19}F per cell. A second batch of glioma cells was labelled at comparable levels with PFPE emulsion without metal. Cells (5×10^6 per side) were injected subcutaneously into the left (no metal) and right (FETRIS) flanks in syngeneic C57BL/6 mice ($N = 3$). After 24 h, mice were imaged with $^1H/^{19}F$ MRI at 11.7 T (Fig. 6b). The ^{19}F images were acquired using a three-dimensional (3D) ZTE sequence (Fig. 6b). Cells were readily visible (SNR ~ 7) in the right injected flank (Fig. 6b), but not on the left side (no metal). Future *in vivo* studies will utilize FETRIS to image stem cells and immune cell populations in preclinical models.

Outlook

Here we present a unique approach for formulating nanoemulsions using PFPE-based β-diketones (FDKs) as metal chelators. These ligands have previously been studied in the context of material science[16], NMR spectroscopy[22] and catalysis[23]. We show that FDK is well suited for incorporating large amounts of paramagnetic metal ions into the fluorous liquids. Formulated as stable PFPE-in-water nanoemulsions, FDKs efficiently and irreversibly extract Fe^{3+} ions from aqueous solution into the fluorous phase, giving rise to a cytocompatible FETRIS agent. These paramagnetic materials are useful for ^{19}F MRI with enhanced sensitivity owing to a marked reduction in T_1, a fundamental parameter limiting the speed of MRI data acquisitions. The ^{19}F T_1 value reduction is magnetic field strength dependent, but can potentially be accelerated to values approaching ×80 at clinical field strengths, yielding a >8-fold sensitivity increase in ^{19}F detection; these sensitivity increases diminish at higher magnetic field strengths (Supplementary Fig. 12). We show that FETRIS is effective for ^{19}F MRI using conventional MRI pulse sequences.

Gd^{3+} and Fe^{3+} are at the heart of T_1- and T_2-based ^1H contrast agents, respectively, but for ^{19}F MRI, the roles of these metal ions are reversed. Fe^{3+} was the optimal T_1 enhancer for perfluorocarbons, whereas analogous gadolinium (and manganese) chelates caused severe line broadening, essentially becoming ^{19}F T_2 agents. Paramagnetic relaxation enhancement has been previously applied to ^{19}F nuclei[7,20,24,25]. ^{19}F MR probes based on macrocyclic lanthanide complexes with fluorinated substituents have been described[7,20]. However, these paramagnetic ^{19}F tracers are not ideal for cell detection purposes. The relatively low ^{19}F content of osmotically active macrocyclic chelates makes it difficult to reach MR-detectable cell loadings compared with highly fluorinated PFC oils. In other approaches, Gd macrocyclic chelates bound to nanoemulsion surface can be used to provide a modest enhancement of ^{19}F T_1, but these are unstable in the intracellular milieu, especially if they traffic to low pH compartments[26], which tends to separate the chelate from the nanoemulsion droplet, thereby limiting long-term enhancement. In contrast, FETRIS complexes are characterized by very small rates of metal leakage even in the presence of EDTA *in vitro* and after cell labelling. The toxicity testing of FETRIS as reported here is viewed as preliminary; more rigorous *in vitro* cell studies, as well as animal testing, are

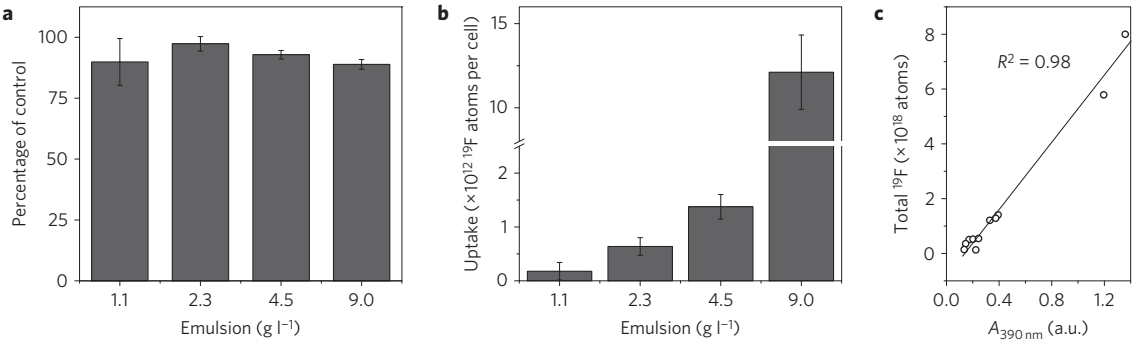

Figure 5 | Cell labelling with FETRIS nanoemulsion. Cells (GL261) were labelled in culture using FETRIS nanoemulsion. **a**, Cell viability. **b**, Cell uptake of FETRIS as measured by ^{19}F NMR. **c**, Correlation of uptake determined by ^{19}F NMR with optical absorbance (A) of cell lysate at 390 nm due to FETRIS. Error bars are standard deviations from three independent replicates.

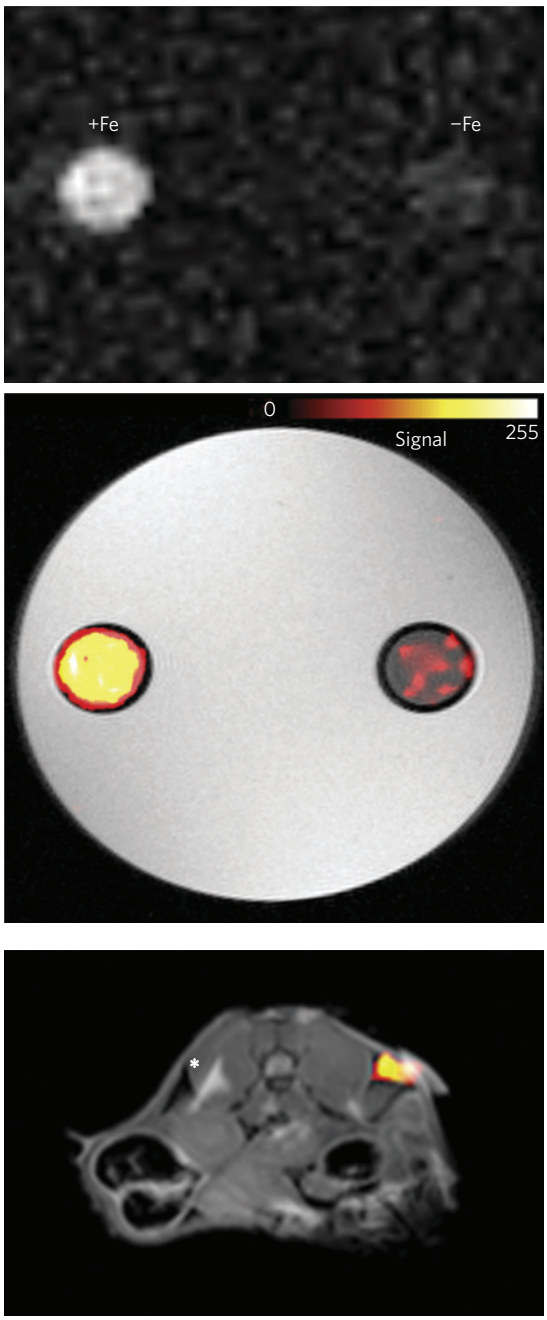

Figure 6 | MRI of FETRIS nanoemulsion. a, Phantom comprised of two agarose-embedded NMR tubes containing FETRIS nanoemulsion (4.5 g l^{-1} ^{19}F) with 0.5 mM Fe^{3+} ($R_1/R_2 = 32.5/170\ s^{-1}$) and nanoemulsion without metal ($R_1/R_2 = 2.2/3.7\ s^{-1}$), denoted +Fe and −Fe, respectively. The top panel shows unthresholded ^{19}F images, and below, the ^{19}F image is thresholded, rendered in hot-iron pseudo-colour (scale bar), and overlaid onto the greyscale ^{1}H image. The ^{19}F/^{1}H MRI data were acquired using a gradient echo (GRE) sequence. **b**, Mouse GL261 glioma cells (5×10^6), labelled with FETRIS nanoemulsion *ex vivo*, were subcutaneously injected into mouse flank. The ^{19}F data are rendered in pseudo-colour and placed on a greyscale slice from the ^{1}H data. After 24 h, mice were imaged and a cell 'hotspot' is seen on the right flank in the axial view. Cells labelled with metal-free nanoemulsion and injected on the contralateral side could not be detected. The asterisk marks an adjacent chemical shift displacement artefact from hyperintense subcutaneous fat at 11.7 T. The ^{19}F and ^{1}H images were acquired using ZTE and GRE pulse sequences, respectively. For display, a co-registered 2D GRE slice was embedded into a 3D rendering of the ^{19}F data.

needed to determine potential suitability for clinical trials. We note that emerging ^{1}H MRI techniques such as PARACEST (ref. 27) and highly shifted proton MRI (ref. 28) have shown promise to detect multiple cell populations on standard MRI instrumentation with high specificity.

Overall, ^{19}F MRI cell detection using PFC tracer agents is a rapidly emerging alternative to ^{1}H-based approaches using metal-ion-based contrast agents. The technical barriers associated with implementation of ^{19}F MRI on a clinical scanner are surmountable, and clinical ^{19}F cell detection has recently been demonstrated[5]. Future improvements in sensitivity of the probes will only accelerate adoption of this technology and open up new uses for this technology; towards this goal, the excellent stability and unique magnetic properties of FETRIS should advance this field.

Methods

Methods and any associated references are available in the online version of the paper.

Received 13 August 2015; accepted 26 January 2016; published online 14 March 2016

References

1. Ahrens, E. T. & Bulte, J. W. M. Tracking immune cells *in vivo* using magnetic resonance imaging. *Nature Rev. Immunol.* **13,** 755–763 (2013).
2. Ahrens, E. T., Flores, R., Xu, H. Y. & Morel, P. A. *In vivo* imaging platform for tracking immunotherapeutic cells. *Nature Biotechnol.* **23,** 983–987 (2005).
3. Srinivas, M., Morel, P. A., Ernst, L. A., Laidlaw, D. H. & Ahrens, E. T. Fluorine-19 MRI for visualization and quantification of cell migration in a diabetes model. *Magn. Reson. Med.* **58,** 725–734 (2007).
4. Srinivas, M. *et al*. *In vivo* cytometry of antigen-specific T cells using ^{19}F MRI. *Magn. Reson. Med.* **62,** 747–753 (2009).
5. Ahrens, E. T., Helfer, B. M., O'Hanlon, C. F. & Schirda, C. Clinical cell therapy imaging using a perfluorocarbon tracer and fluorine-19 MRI. *Magn. Reson. Med.* **72,** 1696–1701 (2014).
6. Neubauer, A. M. *et al*. Gadolinium-modulated F-19 signals from perfluorocarbon nanoparticles as a new strategy for molecular imaging. *Magn. Reson. Med.* **60,** 1066–1072 (2008).
7. Schmid, F., Höltke, C., Parker, D. & Faber, C. Boosting 19F MRI—SNR efficient detection of paramagnetic contrast agents using ultrafast sequences. *Magn. Reson. Med.* **69,** 1056–1062 (2013).
8. de Vries, A. *et al*. Relaxometric studies of gadolinium-functionalized perfluorocarbon nanoparticles for MR imaging. *Contrast Media Mol. Imaging* **9,** 83–91 (2014).
9. Brown, R. W., Cheng, Y. C. N., Haacke, E. M., Thompson, M. R. & Venkatesan, R. *Magnetic Resonance Imaging: Physical Prinicples and Sequence Design* 2nd edn (Wiley, 2014).
10. Hu, L., Zhang, L., Chen, J., Lanza, G. M. & Wickline, S. A. Diffusional mechanisms augment the fluorine MR relaxation in paramagnetic perfluorocarbon nanoparticles that provides a 'relaxation switch' for detecting cellular endosomal activation. *J. Magn. Reson. Imaging* **34,** 653–661 (2011).
11. Solomon, I. Relaxation processes in a system of two spins. *Phys. Rev.* **99,** 559–565 (1955).
12. Bloembergen, N. & Morgan, L. O. Proton relaxation times in paramagnetic solutions. Effects of electron spin relaxation. *J. Chem. Phys.* **34,** 842–850 (1961).
13. Marchionni, G., Ajroldi, G., Righetti, M. C. & Pezzin, G. Molecular interactions in perfluorinated and hydrogenated compounds: linear paraffins and ethers. *Macromolecules* **26,** 1751–1757 (1993).
14. Lai, C.-Z., Reardon, M. E., Boswell, P. G. & Bühlmann, P. Cation-coordinating properties of perfluoro-15-crown-5. *J. Fluor. Chem.* **131,** 42–46 (2010).
15. Shibata, S., Onuma, S. & Inoue, H. Crystal and molecular structure of trimeric bis(acetylacetonato)manganese(II). *Inorg. Chem.* **24,** 1723–1725 (1985).
16. Binnemans, K. in *Handbook on the Physics and Chemistry of Rare Earths* Vol. 35 (eds Karl, J.-C. G. B., Gschneidner, A. & Vitalij, K. P.) 107–272 (Elsevier, 2005).
17. Barkley, L. B. & Levine, R. The synthesis of certain ketones and α-substituted β-diketones containing perfluoroalkyl groups. *J. Am. Chem. Soc.* **75,** 2059–2063 (1953).
18. Janjic, J. M. & Ahrens, E. T. Fluorine-containing nanoemulsions for MRI cell tracking. *Wiley Int. Rev. Nanomed. Nanobiotechnol.* **1,** 492–501 (2009).
19. Lintvedt, R. L. & Kernitsky, L. K. Ligand field information from charge-transfer spectra of substituted tris(1,3-diketonato)iron(III) chelates. Spectrochemical series for 1,3-diketones. *Inorg. Chem.* **9,** 491–494 (1970).

20. Funk, A. M., Fries, P. H., Harvey, P., Kenwright, A. M. & Parker, D. Experimental measurement and theoretical assessment of fast lanthanide electronic relaxation in solution with four series of isostructural complexes. *J. Phys. Chem. A* **117,** 905–917 (2013).
21. Nash, K. L., Brigham, D., Shehee, T. C. & Martin, A. The kinetics of lanthanide complexation by EDTA and DTPA in lactate media. *Dalton Trans.* **41,** 14547–14556 (2012).
22. Sanders, J. K. M., Hanson, S. W. & Williams, D. H. Paramagnetic shift reagents. Nature of the interactions. *J. Am. Chem. Soc.* **94,** 5325–5335 (1972).
23. Lo, J. C., Gui, J., Yabe, Y., Pan, C.-M. & Baran, P. S. Functionalized olefin cross-coupling to construct carbon–carbon bonds. *Nature* **516,** 343–348 (2014).
24. Harvey, P., Kuprov, I. & Parker, D. Lanthanide complexes as paramagnetic probes for ^{19}F magnetic resonance. *Eur. J. Inorg. Chem.* **2012,** 2015–2022 (2012).
25. De Luca, E. *et al*. Characterisation and evaluation of paramagnetic fluorine labelled glycol chitosan conjugates for F-19 and H-1 magnetic resonance imaging. *J. Biol. Inorg. Chem.* **19,** 215–227 (2014).
26. Kok, M. B. *et al*. Quantitative H-1 MRI, F-19 MRI, and F-19 MRS of cell-internalized perfluorocarbon paramagnetic nanoparticles. *Contr. Media Mol. Imaging* **6,** 19–27 (2011).
27. Ferrauto, G., Castelli, D. D., Terreno, E. & Aime, S. *In vivo* MRI visualization of different cell populations labeled with PARACEST agents. *Magn. Reson. Med.* **69,** 1703–1711 (2013).
28. Schmidt, R. *et al*. Highly shifted proton MR imaging: cell tracking by using direct detection of paramagnetic compounds. *Radiology* **272,** 785–795 (2014).

Acknowledgements

This work was financially supported by National Institutes of Health grants T32-CA121938 (UCSD Cancer Therapeutics Training Program, A.A.K.), R01-CA158448 (R.Y.T.) and R01-EB017271 (E.T.A.), Radiological Society of North America grant RR1452 (K.H.N), and California Institute for Regenerative Medicine grant LA1-C12-06919 (E.T.A.). We thank T. C. Nguyen, M. J. Patrick, A. Waggoner, A. Mrse, T. Didenko, P. McConville and K. Wuthrich for technical assistance, and V. Kislukhin for helpful discussions.

Author contributions

A.A.K. designed synthesis schemes, performed chemical synthesis of the molecules and emulsions, characterized synthesis products, and wrote the first draft of the manuscript. H.X. performed tissue culture experiments. S.R.A. helped design experiments, performed chemical synthesis, and helped edit the manuscript. K.H.N. assisted with the *in vivo* animal experiments and MRI renderings and helped edit the manuscript. R.Y.T. helped design experiments and edit the manuscript. E.T.A. helped design experiments, acquired MRI data in phantoms and in mice, edited the final version of the manuscript.

Additional information

Supplementary information is available in the online version of the paper. Reprints and permissions information is available online at www.nature.com/reprints. Correspondence and requests for materials should be addressed to R.Y.T. or E.T.A.

Competing financial interests

The authors declare no competing financial interests.

Methods

Emulsion preparation. The fluorocarbon oil blends were prepared from PFPE, PFPE-DEA (Exfluor), PFOB (Acros) and pAn-FDK (see Supplementary Methods for synthetic procedures) agents. Proportions (Fig. 2) were prepared gravimetrically in a 15 or 50 ml conical Falcon tube (Corning). Per 1 g of PFC blend, 0.5 ml aqueous solution of Pluronic F68 (100 $g\,l^{-1}$) was added, and the mixture was vortexed at the highest speed. Water (8.5 ml) was added, followed by brief vortexing and ultrasonication (Omni Ruptor 250 W, 30% power, 2 min, Omni International). The crude emulsion thus obtained was passed 4–6 times through an LV1 microfluidizer (Microfluidics) operating at 20,000 psi and filtered through a 0.2 μm Supor membrane (Pall Corp. no. 4187) into sterile glass vials.

NMR measurements. NMR spectra were obtained on Magritek Spinsolve (1.0 T), Bruker Avance 300 (7.0 T), Bruker Ascend 400 (9.4 T), Jeol ACA 500 (11.7 T) and Bruker DRX-600 (14.1 T) instruments. ^{19}F NMR spectra of aqueous nanoemulsions were referenced to an internal standard (0.1 wt% CF_3CO_2Na/D_2O, −76.00 ppm), which served as the integration reference for quantitative NMR (see Supplementary Information). Relaxation measurements were performed using a standard inversion recovery (with TI, time to inversion, from 3^{-2} to 3^9 ms) pulse sequence and a Carr–Purcell–Meiboom–Gill sequence with TE (echo time) values in 12 linear increments. R_1 and R_2 were obtained by nonlinear fitting in MNova 6.0.2 software (Mestrelab). Fit errors were less than 5% for R_1 and 10% for R_2.

Cell labelling. Rat 9L or mouse GL261 glioma cells ($3–5 \times 10^6$, ATCC; no authentication or mycoplasma testing was performed) were plated in 10 cm dishes and allowed to attach overnight. Immediately before cell labelling, FDK (B or D) or control (C or E) emulsion (0.5 ml) was mixed with freshly prepared $FeCl_3$ (50 mM in H_2O, 0.12 ml), protamine sulfate (1% in H_2O, 0.02 ml) and Tris base (1 M in H_2O, 0.25 ml). The dark-orange liquid was diluted to the desired PFPE content with DMEM (9L) or RPMI-1640 (GL261) medium supplemented with 10% (v/v) fetal bovine serum. Labelling medium was added to cells at 5 ml per dish. After 16 h incubation at 37 °C, the cell labelling medium was removed, and cells were washed three times with phosphate-buffered saline (PBS), detached by trypsinization, washed again in PBS, and resuspended in 1 ml of PBS. A portion of the cell suspension (∼1/10) was used for cell number estimates by Cell Titer Glo (Promega) or using a Countess II FL Cell Counter (Life Technologies). To assay nanoemulsion uptake, cells were pelleted and resuspended in 0.1 ml of lysis solution (0.5% Triton X, 100 mM NaCl, 20 mM Tris). A portion of this solution (6 μl) was used for absorbance measurements on a NanoDrop 2000 spectrophotometer (Thermo Scientific). The remainder was transferred to a 5 mm NMR tube, mixed with 0.15 ml of 0.1 wt% CF_3CO_2Na/D_2O reference compound and ^{19}F NMR spectra were obtained to measure ^{19}F uptake, as previously described[29].

MRI. A phantom sample was prepared using 5 mm NMR tubes containing FETRIS ($4.5\,g\,l^{-1}$ ^{19}F, 0.5 mM Fe^{3+}, $R_1/R_2 = 32.5/170\ s^{-1}$) and nanoemulsion without metal ($R_1/R_2 = 2.2/3.7\ s^{-1}$); tubes were embedded in agarose. All images were acquired using a Bruker 11.7 T BioSpec using a ^{19}F/^{1}H double-tuned volume coil. For ^{19}F, a gradient echo (GRE) pulse sequence was used with parameters: TR/TE = 15/0.83 ms (TR: recovery time), NA = 256 (NA: number of averages), FOV = 4 × 4 cm (FOV: field of view), 64 × 64 matrix, 8-mm-thick slices, and a ∼4 min data acquisition time. In this image, the TE parameter was minimized to 0.83 ms, but at this value there is a residual amount of signal attenuation from T_2 effects in the FETRIS material (estimated ∼12%). We used the Ernst angle condition[9] for optimal ^{19}F imaging of the FETRIS phantom. For ^{1}H, the GRE parameters were TR/TE = 150/2 ms, NA = 8, FOV = 4 × 4 cm, 256 × 256 matrix, and 2 mm slices. The ^{19}F image data were rendered in hot-iron pseudo-colour using ImageJ software (NIH) and overlaid onto the greyscale ^{1}H image. For *in vivo* mouse studies, mouse GL261 glioma cells were labelled with FETRIS nanoemulsion (50 wt% pAn-FDK, 50 wt% PFPE) *ex vivo* to a level of $\sim 10^{12}$ ^{19}F per cell. A second batch of cells was similarly labelled but with unmetallated nanoemulsion. Cells (5×10^6 per side) were injected subcutaneously into flanks in female syngeneic C57BL/6 mice (8–10 weeks old, $N = 3$) using a vehicle of 0.2 ml Matrigel (BD Biosciences) in PBS. The FETRIS-labelled cells, and cells labelled with unmetallated nanoemulsion, were injected into the right and left sides, respectively. After 24 h, mice were imaged using a 3D ZTE sequence with parameters TR = 4 ms, receiver bandwidth 40 kHz, acquisition window 0.8 ms, number of projections 13,030, NA = 26, acquisition time 23 min, FOV = 6 × 6 × 6 cm, and matrix size 64 × 64 × 64. Proton data were acquired using a 2D spin-echo sequence with TR/TE = 1,500/14 ms, FOV = 6 × 6 cm, and 256 × 256 matrix. ^{19}F data were imported into Amira software (FEI) and rendered in colour and a greyscale slice from the ^{1}H data was embedded for anatomical display purposes.

References

29. Janjic, J. M., Srinivas, M., Kadayakkara, D. K. K. & Ahrens, E. T. Self-delivering nanoemulsions for dual fluorine-19 MRI and fluorescence detection. *J. Am. Chem. Soc.* **130,** 2832–2841 (2008).